

Excitons and light-emission in semiconducting MoSi₂X₄ two-dimensional materials

Original

Excitons and light-emission in semiconducting MoSi₂X₄ two-dimensional materials / Sun, MI; Re Fiorentin, M; Schwingenschlogl, U; Palummo, M. - In: NPJ 2D MATERIALS AND APPLICATIONS. - ISSN 2397-7132. - ELETTRONICO. - 6:1(2022). [10.1038/s41699-022-00355-z]

Availability:

This version is available at: 11583/2974212 since: 2023-01-12T16:33:50Z

Publisher:

NATURE PORTFOLIO

Published

DOI:10.1038/s41699-022-00355-z

Terms of use:

This article is made available under terms and conditions as specified in the corresponding bibliographic description in the repository

Publisher copyright

(Article begins on next page)

ARTICLE OPEN

Excitons and light-emission in semiconducting MoSi_2X_4 two-dimensional materialsMinglei Sun^{1,4}, Michele Re Fiorentin^{2,4}, Udo Schwingenschlög¹✉ and Maurizia Palummo³✉

Semiconducting two-dimensional materials with chemical formula MoSi_2X_4 ($\text{X} = \text{N}, \text{P}, \text{or As}$) are studied by means of atomistic ground- and excited-state first-principles simulations. Full-fledged quasi-particle bandstructures within the G_0W_0 approach substantially correct the electronic bandgaps previously obtained with hybrid-functional density functional theory and highlight the absence of lateral valleys close in energy to the conduction band minimum. By solving the Bethe–Salpeter equation, we show that the optical properties are dominated by strongly bound excitons with the absorbance and maximum short-circuit current densities of MoSi_2P_4 and MoSi_2As_4 comparable to those of transition metal dichalcogenides. Due to the presence of the outer SiX layers, the exciton binding energies are smaller than those generally found for transition metal dichalcogenides. Long radiative lifetimes of bright excitons, over 10 ns at room temperature for MoSi_2As_4 , and the absence of band-nesting are very promising for application in efficient ultra-thin optoelectronic devices.

npj 2D Materials and Applications (2022)6:81 ; <https://doi.org/10.1038/s41699-022-00355-z>

INTRODUCTION

Atomically thin two-dimensional (2D) materials are nowadays the subject of intense fundamental and technological research^{1–6}. Due to the reduced dimensionality and the weak dielectric screening, their opto-electronic response, even at room temperature, is dominated by strongly bound electron-hole pairs, called excitons⁷. Among a plethora of semiconducting 2D materials, the family of group VI transition metal dichalcogenides (TMDs) is most attractive for very high absorbance and optical bandgaps ranging from the visible to the near-infrared region of the electromagnetic spectrum^{8,9}. TMDs thus are promising candidates for next generation opto-electronic and photonic devices, such as photovoltaic solar cells^{10,11}, photodetectors^{12,13}, and light-emitting diodes¹⁴. However, the opto-electronic performance of TMDs is affected by spin and momentum-forbidden dark excitons. The former originate from the strong spin-orbit coupling at the K and K' points^{15,16}, the latter are mainly due to the presence of lateral valleys at the Λ (or Q) point, midway between the Γ and K points of the Brillouin zone¹⁷. Their energy ordering relative to the bright direct K-K excitons has a profound impact on the photoluminescence efficiency. A spin-forbidden dark exciton as lowest-energy state, as in WS_2 , and finite momentum excitons energetically close to the bright exciton, as in MoS_2 , introduce additional non-radiative decay channels that hamper the photoluminescence quantum yield¹⁷.

The 2D semiconducting material MoSi_2N_4 recently has been synthesized by chemical vapor deposition¹⁸. It has a layered structure with P6m2 space group, in which an inner MoN_2 layer is coordinated to two outer SiN layers, compare Fig. 1. It exhibits an indirect band gap, a high strength (66 GPa), and remarkable ambient stability. Theoretical calculations based on the deformation potential approach predict high intrinsic electron and hole mobilities of $270 \text{ cm}^2 \text{ V}^{-1} \text{ s}^{-1}$ and $1200 \text{ cm}^2 \text{ V}^{-1} \text{ s}^{-1}$, respectively^{18,19}, which result in a high on/off ratio of 4000 at 77 K in a back-gated field-effect transistor. The carrier type and bandgap of

MoSi_2N_4 can be easily manipulated by doping²⁰. Interestingly, other 2D materials with the general formula MoSi_2X_4 and the same structure as MoSi_2N_4 can be obtained by elemental substitution and exhibit versatile properties²¹. The indirect bandgap becomes direct after replacing the N atoms by P or As atoms^{22,23}. The absence of inversion symmetry in the structure of MoSi_2X_4 allows for valley polarization by optical pumping with circularly polarized light^{22,24}, making the materials suitable for application in spintronics and valleytronics²¹. Several members of the family exhibit high piezoelectric coefficients and are predicted to show high lattice thermal conductivity, comparable with Cu²⁵.

Despite the appeal of the materials, theoretical investigations in the literature have focused on the electronic and optical properties^{22,26,27} mainly within the limited density functional theory (DFT) approach. It is known that DFT fails at properly predicting both the electronic bandgap of semiconductors and the light absorption spectra. In particular, DFT intrinsically misses the excitonic features that are essential in low-dimensional materials. For this reason, in this work, we study MoSi_2X_4 ($\text{X} = \text{N}, \text{P}, \text{or As}$) employing state-of-the-art many-body perturbation theory techniques, to disclose the excitonic nature of the optical properties, which inevitably must be taken into account to provide thorough insights into the basic properties of these materials and reliable guidance to future experimental works.

RESULTS AND DISCUSSION

Structure and electronic properties

Figure 1 shows the relaxed atomic structures of MoSi_2N_4 , MoSi_2P_4 , and MoSi_2As_4 . Their optimized lattice constants are 2.91, 3.47, and 3.62 Å, respectively, in agreement with previous reports^{18,27}. The PBE and G_0W_0 band structures are reported in Fig. 2. We confirm that MoSi_2N_4 is an indirect bandgap semiconductor both at the PBE and G_0W_0 levels, with the valence band maximum (VBM) located at the Γ point and the conduction band minimum (CBM)

¹Applied Physics Program, Physical Science and Engineering Division, King Abdullah University of Science and Technology (KAUST), Thuwal, Saudi Arabia. ²Center for Sustainable Future Technologies, Istituto Italiano di Tecnologia, Torino, Italy. ³Dipartimento di Fisica and INFN, Università di Roma “Tor Vergata”, Roma, Italy. ⁴These authors contributed equally: Minglei Sun, Michele Re Fiorentin. ✉email: udo.schwingenschlög@kaust.edu.sa; maurizia.palummo@roma2.infn.it

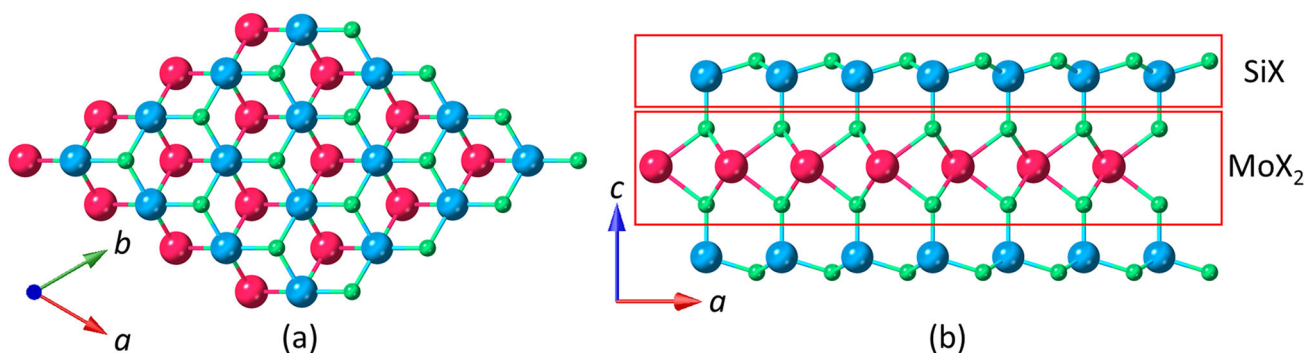


Fig. 1 Atomic structure. Top **a** and side **b** views. In **b** the MoX₂ and SiX layers are marked. The violet, blue, and green spheres are Mo, Si, and X atoms, respectively.

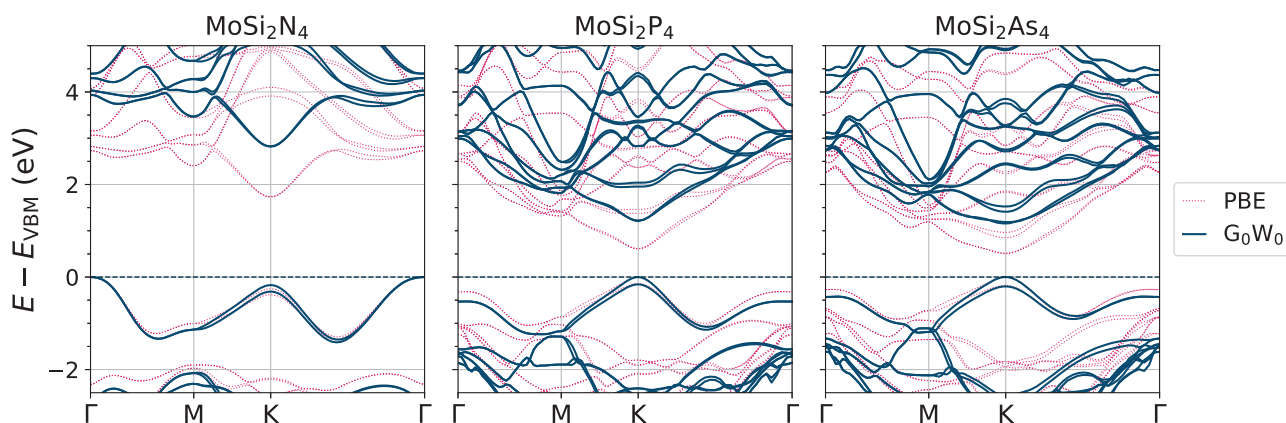


Fig. 2 Band structures. The energies refer to the VBM.

located at the K point. Both the valence and conduction band edges are split due to spin-orbit coupling and lack of inversion symmetry. The valence band edge at the K point shows a splitting of 158 (141) meV at the G_0W_0 (PBE) level, while the conduction band edge shows a much smaller splitting of 10 (3) meV. The G_0W_0 bandgap is 2.79 eV, i.e., 1.02 eV larger than the PBE bandgap. The direct gap at the K point is 2.96 eV, i.e., 0.18 eV larger than the indirect bandgap. In MoSi₂P₄ and MoSi₂As₄ the bandgaps turn direct with the VBM shifting to the K point. The splittings at the VBM and CBM are much larger than for MoSi₂N₄, specifically, 158 (139) and 14 (4) meV for MoSi₂P₄ and 203 (181) and 28 (16) meV for MoSi₂As₄ at the G_0W_0 (PBE) level due to the heavier masses of P and As. The G_0W_0 bandgap is 1.17 eV for MoSi₂P₄ and 1.01 eV for MoSi₂As₄. As a comparison, the HSE06 hybrid functional²⁷ underestimates the direct bandgap with respect to the G_0W_0 bandgap by about 0.35 eV for MoSi₂P₄ and MoSi₂As₄ and by 0.65 eV for MoSi₂N₄. This fact has sizeable implications on the optical properties of the materials. It is worth mentioning that the G_0W_0 bandgaps of MoSi₂X₄ are inversely proportional to the atomic number of the X element, as explained by the decreasing electronegativity.

Figure 2 also displays a first significant difference from traditional TMDs. The absence of lateral valleys (e.g., the Λ valleys in TMDs) along the Γ -K high-symmetry direction. Due to the absence of Λ valleys close in energy to the K valleys, excitons have fewer non-radiative recombination channels in MoSi₂X₄ than in TMDs, hinting at a less suppressed quantum yield and high efficiencies in optoelectronic devices. It recently has been proven that non-radiative recombination channels can be efficiently suppressed in TMDs by electrostatic doping²⁸ and strain²⁹. We

anticipate that the same approaches can be applied to further enhance the quantum yield of MoSi₂X₄ (X = N, P, or As).

Optical properties

In the upper panels of Fig. 3 we report the absorption spectra computed at the BSE level. The absorption onset falls in the visible region for MoSi₂N₄, at 2.31 eV, and in the near infrared region at 0.77 and 0.71 eV for MoSi₂P₄ and MoSi₂As₄, respectively. The overlap of the absorption spectra with the incident AM1.5G solar flux $\Phi_s(\omega)$ (shaded gray region in Fig. 3), while limited for MoSi₂N₄, is larger for MoSi₂P₄ and MoSi₂As₄. To quantify the theoretical efficiency of the absorption of solar light we compute the maximum short-circuit current density as $J_{sc}^{max} = e \int d\omega A(\omega) \Phi_s(\omega)$, where $A(\omega)$ is the absorbance¹¹. The value of J_{sc}^{max} is only 0.7 mA/cm² in the case of MoSi₂N₄, while MoSi₂P₄ and MoSi₂As₄ exhibit large values of 3.6 and 4.5 mA/cm², respectively, because of the lower absorption onset. These values are comparable with well-studied TMDs³⁰, such as MoS₂ (3.9 mA/cm²) and MoSe₂ (4.6 mA/cm²), indicating great potential of MoSi₂X₄ in photovoltaic applications.

Exciton fine structure

Selected absorption peaks A, B, \tilde{B} , and C are marked in the upper panels of Fig. 3, with the electronic transitions taking place at the k -points correspondingly highlighted in the lower panels. Similarly to TMDs, peaks A and B are due to well-defined excitons with contributions from transitions at the K and K' points, reflecting the band splitting induced by the spin-orbit coupling. As shown in more detail for MoSi₂P₄ in Fig. 4a–c, excitons A and B originate

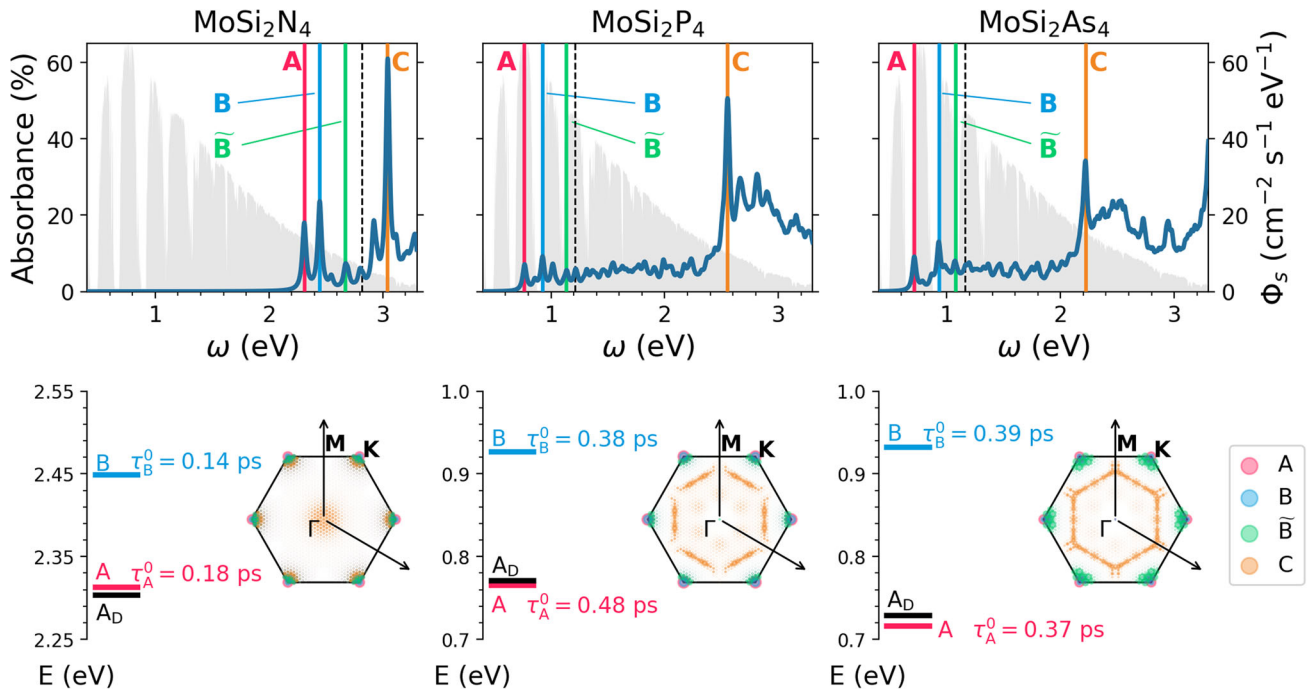


Fig. 3 Absorption spectra and exciton radiative lifetimes. Upper panels: Absorption spectra computed at the BSE level. The dashed vertical lines mark the G_0W_0 bandgaps. Lower panels: Intrinsic radiative lifetimes of excitons A and B at 0 K, and exciton weights in the Brillouin zone. A_D denotes the dark exciton.

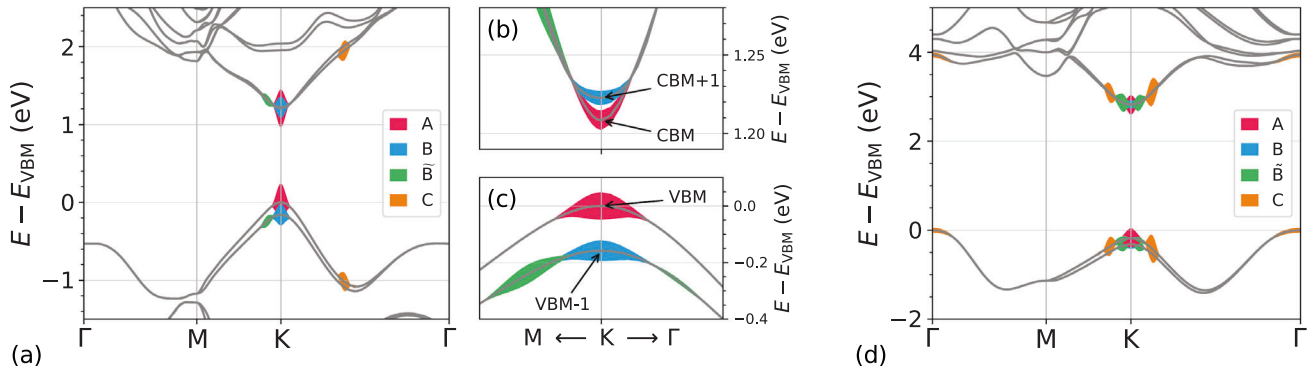


Fig. 4 Weighted band structures. G_0W_0 bandstructure of **a** MoSi_2P_4 and **d** MoSi_2N_4 with weights of the single-particle transitions giving rise to excitons A, B, \tilde{B} , and C (Fig. 3). In **b** and **c** we report details of the CBM(+1) and VBM(-1), respectively, around the K point.

from the allowed transitions between same-spin bands, namely $\text{VBM} \rightarrow \text{CBM}$ for exciton A and $\text{VBM}-1 \rightarrow \text{CBM}+1$ for exciton B. The binding energy of exciton A is 0.68 eV in MoSi_2N_4 and 0.44 eV in both MoSi_2P_4 and MoSi_2As_4 , i.e., smaller than the binding energy of the lowest-energy bright exciton of a MoS_2 monolayer, estimated to be larger than 0.70 eV at the same level of theory^{31,32}. Excitons A and B in the case of MoSi_2N_4 are located at 2.31 and 2.45 eV, respectively, in agreement with the experimental values (2.21 and 2.35 eV)¹⁸. The 0.1 eV blueshift of the computed exciton energies with respect to the experimental values can be attributed to three main effects that were not included in the calculations: the presence of a substrate, which has been shown to reduce the optical gap of single-layer TMDs by up to 0.1 eV^{33,34}, temperature effects, which already at 0 K cause a redshift of 75 meV in single-layer MoS_2 due to zero-point renormalization³⁵, and tensile strain, which has a strong impact on the band structure of MoSi_2N_4 already at small magnitudes (see Supplementary Fig. 4).

Spin-forbidden transitions between opposite-spin bands at the K and K' points give rise to the dark exciton A_D with zero dipole moment for in-plane light polarization. Above peaks A and B, it is possible to identify in Fig. 3 several peaks with lower intensities. As a representative, we select a peak \tilde{B} , which is due to $\text{VBM}-1 \rightarrow \text{CBM}+1$ transitions (as peak B) taking place near the K and K' points (Fig. 4). These transitions are slightly more energetic and less intense, as they occur only in the vicinity of the high-symmetry K and K' points.

Finally, we find in Fig. 3 an intense absorption peak at higher energy, well above the G_0W_0 direct bandgap, which originates from direct transitions ($\text{VBM} \rightarrow \text{CBM}$) within the Brillouin zone (lower panels of Fig. 3). We mark it as C to suggest a possible analogy with the intense peaks that are found in TMDs and are mainly given by similar transitions at k -points intermediate between Γ and K. In the case of the TMDs these transitions take place in regions of the Brillouin zone where the valence and conduction bands are almost parallel, i.e., 'nested'³⁶. In such

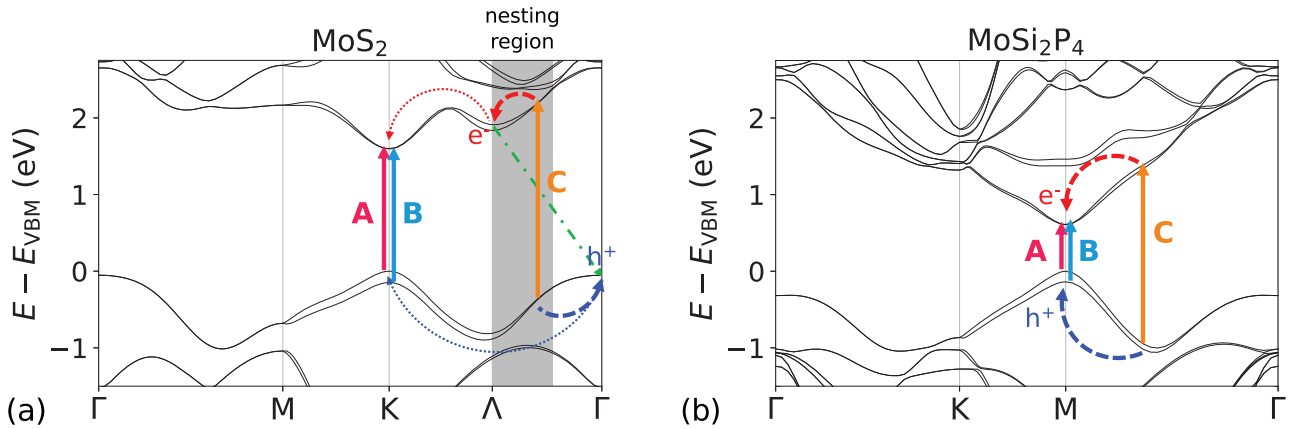


Fig. 5 Relaxation. Relaxation processes of the excited charge carriers from peak C in **a** MoS₂ and **b** MoSi₂P₄.

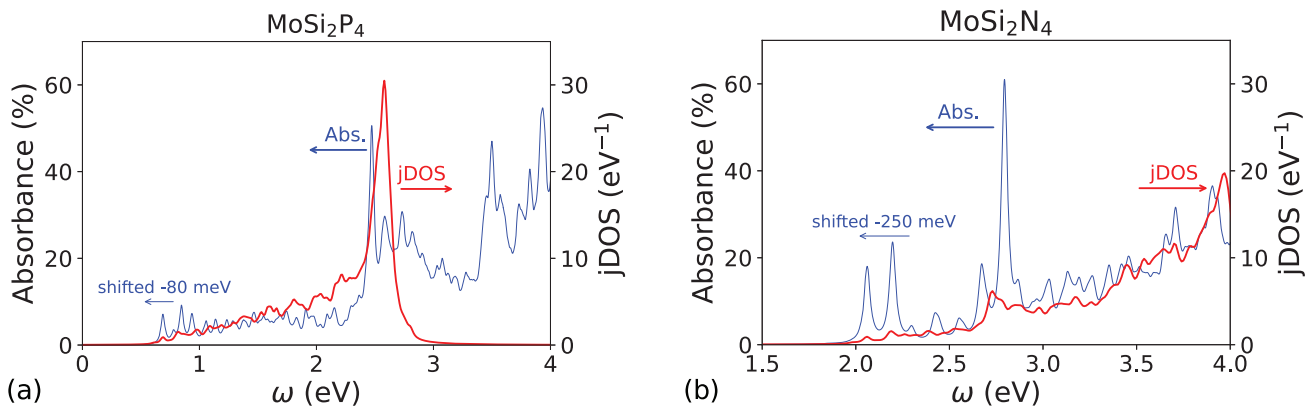


Fig. 6 jDOS and absorbance. jDOS per unit cell (red line) and absorbance (blue line) of **a** MoSi₂P₄ and **b** MoSi₂N₄. The jDOS is obtained from the PBE eigenvalues and only comprises transitions involving the VBM-1, VBM, CBM, and CBM+1. The absorbance is shifted to match the jDOS, as reported in each panel.

conditions, photo-generated electrons and holes relax with opposite momenta to their closest band extrema, i.e., to the Λ valley and Γ hill, respectively. Hence, photo-generated carriers remain separated in momentum space, and the quantum yield drops significantly³⁷. This does not happen for MoSi₂P₄ and MoSi₂As₄ according to Fig. 4, since no lateral valley is interposed between the transitions and the band extrema at the K and K' points. In Fig. 5 we show a schematic of the electron-hole relaxation mechanisms in (a) MoS₂ and (b) MoSi₂P₄. In MoS₂ the excited electrons from peak C quickly relax via intraband scattering to the Λ valley between the Γ and K points (dashed red arrow). Simultaneously, the excited holes relax to the Γ hill (blue dashed arrow). Once relaxed, the charge carriers can follow phonon-mediated radiative recombination (dot-dashed green arrow), or non-radiative recombination, or phonon scattering to the K and K' points (dotted red and blue arrows). Only a relatively small fraction of the photo-excited carriers reaches the K and K' points and recombines radiatively, with moderate yield³⁷. In the cases of MoSi₂P₄ and MoSi₂As₄, see Fig. 5b, the photo-generated electrons and holes are statistically favored to quickly relax to the closest K or K' points, via interband scattering (red and blue dashed arrows). It is not possible to fully exclude relaxation paths leading holes to the Γ hill, however they are disfavored by the longer interband scattering chain.

Band nesting in TMDs results in a large enhancement of the joint density of states (jDOS) and, in turn, in an increased absorbance. In MoSi₂P₄ and MoSi₂As₄ the large intensity of peak C can be similarly traced back to the jDOS, see Fig. 6a. However, this

enhancement is not related to band nesting, see Fig. 4, but rather to the reduced curvature of the valence and conduction bands in the region where the electronic transitions contributing to peak C occur. In MoSi₂N₄ the intense peak C is mainly due to contributions from electronic transitions in the vicinity of K/K', as well as at Γ (see the lower panels of Figs. 3 and 4d). The band structure of MoSi₂N₄ shows flat conduction and valence bands around Γ , which enhance the jDOS and, consequently, the intensity, see Fig. 6b. This feature is absent in MoSi₂P₄ and MoSi₂As₄.

As mentioned, the energetic ordering of excitons A_D and A is crucial for the optoelectronic performance. We have verified that in our calculations the bright-dark splitting $\Delta \equiv E_A - E_{A_D}$ is converged within 2 meV (see Supplementary Fig. 2c). It is important to notice that, while in the case of MoSi₂N₄ the dark exciton A_D is the lowest-energy state, with a bright-dark splitting $\Delta = 9$ meV, the ordering is reversed in the cases of MoSi₂P₄ and of MoSi₂As₄, where we have $\Delta = -3$ and -13 meV, respectively (lower panels of Fig. 3). This is the result of interplay between the splitting of the conduction band due to the spin-orbit coupling and the exchange interaction between the electron and hole in the exciton^{32,38}. Indeed, in all three studied materials the band splitting provides a negative contribution to Δ , since the opposite-spin bands involved in exciton A_D are the VBM and CBM+1, implying that the electronic transitions contributing to exciton A (VBM \rightarrow CBM) are less energetic than those contributing to exciton A_D . On the contrary, the exchange interaction always contributes positively to Δ , lowering the energy of the dark exciton with

respect to the bright exciton. The contribution of the exchange interaction to Δ is found to be between 12 meV (MoSi_2P_4) and 18 meV (MoSi_2N_4), being large enough to overcome the band splitting due to the spin-orbit coupling only in the case of MoSi_2N_4 (positive Δ). The negative Δ implies that MoSi_2P_4 and MoSi_2As_4 will show an enhanced quantum yield at low temperatures, unlike TMDs such as WS_2 , WSe_2 ³⁹, and MoS_2 ^{40,41}. In the case of MoSi_2As_4 , due to the large $\Delta = -13$ meV, the quantum yield is expected to be only moderately suppressed even at room temperature, unlike MoSe_2 with $\Delta = -1$ meV^{16,42}. The energetic ordering of the excitons and bright-dark splitting represent the second main specificity of the materials under consideration with respect to traditional TMDs.

The lower panels of Fig. 3 also give the intrinsic radiative lifetimes of excitons A and B at 0 K, $\tau_{A,B}^0$, which all fall in the range of tenths of ps, in line with the values obtained for 2D TMDs⁴³. As shown in Refs. 43–45, in a 2D material the finite temperature radiative lifetime $\langle\tau_X\rangle(T)$ of exciton X is proportional to $k_B T M_X^*/E_X^2$, where M_X^* and E_X are the effective mass and energy of the exciton at zero momentum, respectively. We report in Table 1 the effective masses of the electrons, holes, and excitons, together with the finite temperature exciton radiative lifetimes calculated at $T = 4$ and 300 K.

The values obtained for MoSi_2N_4 are slightly larger than those of MoS_2 , MoSe_2 , and WSe_2 ⁴⁶. Conversely, the values obtained for MoSi_2P_4 and MoSi_2As_4 are about two orders of magnitude larger. This is primarily due to the combination of low energy ($E_{A,B} < 1$ eV) and high effective mass of the excitons, which enhances the temperature-dependent factor in $\langle\tau\rangle(T)$. Long radiative lifetimes are often associated with exciton localization due to defects or

strain, as observed for TMD monolayers and bilayers^{47,48}, or with interlayer excitons in 2D van der Waals heterostructures of TMDs^{49–51}.

We plot in Fig. 7 the square moduli of the wavefunctions of excitons A, B, \tilde{B} , and C of MoSi_2P_4 . Corresponding results for MoSi_2N_4 and MoSi_2As_4 are reported in Supplementary Figs. 5 and 6, respectively. The hole (white diamond) is kept fixed where the valence band edge has the highest probability density. In all cases, excitons A and B both have a circular shape around the hole. The Bohr radii of excitons A and B are estimated to be, respectively, $a_A = 1.79$ nm and $a_B = 1.76$ nm in MoSi_2P_4 , 0.98 nm and 0.96 nm in MoSi_2N_4 , and 1.65 nm and 1.64 nm in MoSi_2As_4 , in line with the values found in TMDs^{52–54}. Exciton \tilde{B} is more delocalized, and exciton C spreads along the zigzag direction. The side views in Fig. 7 show that excitons A, B, and \tilde{B} are concentrated on the inner MoSi_2 layer, whereas exciton C extends to the outer SiP layers. Exciton C shows a similar delocalization in MoSi_2As_4 , while it does not extend to the outer SiN layers in MoSi_2N_4 .

Exciton-exciton annihilation (strong exciton Auger recombination) is a key technological bottleneck to obtain high quantum yield in TMDs, and the less localized C exciton may enhance the annihilation rate by increasing the annihilation radius^{55–57}. Lee et al.⁵⁸ have employed ultra-flat Au substrates with atomically controlled h-BN spacers to suppress the exciton-exciton interaction and improve the quantum yield of TMDs by an order of magnitude. In MoSi_2X_4 layers, due to the contribution of the excitons in the inner MoX_2 layer, the outer SiX layers can act as the h-BN spacers. Thus, chemical vapor deposition of MoSi_2X_4 on a metallic substrate may directly lead to highly efficient optoelectronic devices.

We provide a state-of-the-art study of the electronic and optical properties of 2D MoSi_2X_4 based on many-body perturbation theory. The G_0W_0 approximation overcomes the drawbacks of DFT, being superior to hybrid-functionals, to achieve reliable electronic band structures and bandgaps. The bandgap of MoSi_2N_4 is indirect, while the bandgaps of MoSi_2P_4 and MoSi_2As_4 are direct at the K point with a bandgap value of around 1 eV. Unlike traditional TMDs, they have no lateral valleys close in energy to the CBM. By solving the Bethe-Salpeter equation, we obtain absorption spectra displaying excitonic features. The absorption onset falls into the visible region for MoSi_2N_4 , and into the near-infrared region for MoSi_2P_4 and MoSi_2As_4 , resulting, together with a strong light-carrier coupling, in a significant absorption of the solar flux and in maximum short-circuit current densities comparable to those of TMDs. The analysis of the exciton fine-structure reveals a crucial interplay between the band splitting induced by the spin-orbit coupling and the exchange interaction within the exciton, which results in a bright lowest-

Table 1. Effective exciton masses and finite temperature radiative lifetimes.

| | MoSi_2N_4 | | MoSi_2P_4 | | MoSi_2As_4 | |
|-----------------------------------|---------------------------|------|---------------------------|------|----------------------------|------|
| | A | B | A | B | A | B |
| $M^*(m_0)$ | 0.79 | 1.30 | 0.47 | 1.05 | 1.94 | 1.12 |
| $m_e^*(m_0)$ | 0.28 | 0.74 | 0.18 | 0.69 | 1.51 | 0.58 |
| $m_h^*(m_0)$ | 0.51 | 0.56 | 0.29 | 0.36 | 0.42 | 0.54 |
| $\langle\tau\rangle$ (4 K) (ps) | 7 | 8 | 100 | 123 | 372 | 133 |
| $\langle\tau\rangle$ (300 K) (ns) | 1 | 1 | 7 | 9 | 28 | 10 |

The effective exciton masses are obtained from the G_0W_0 bandstructure and reported in units of the electron rest mass m_0 . The finite temperature radiative lifetimes are computed for excitons A and B at 4 and 300 K.

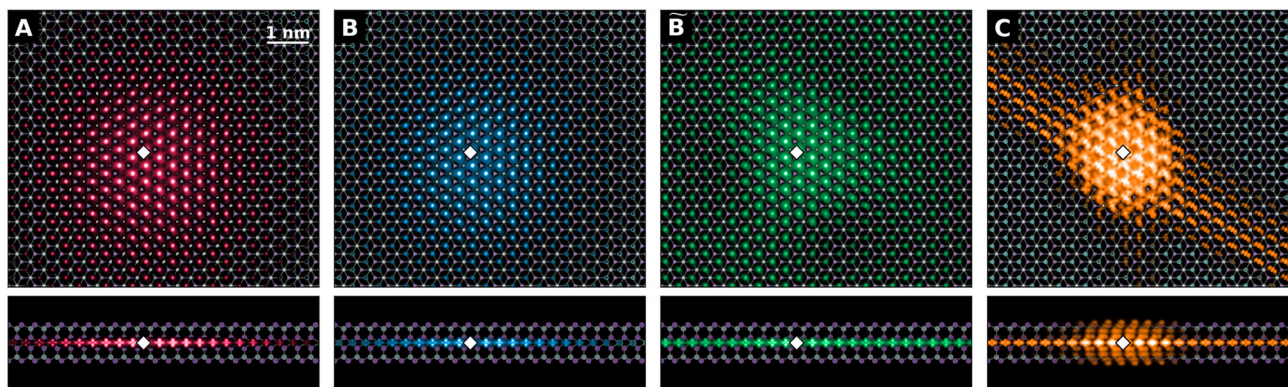


Fig. 7 Wavefunctions. Top (upper panels) and side (lower panels) views of the square moduli of the wavefunctions of excitons A, B, \tilde{B} , and C in MoSi_2P_4 . The white diamond marks the highest probability density of the hole.

energy exciton for both MoSi_2P_4 and MoSi_2As_4 . The negative bright-dark splitting is particularly large (-13 meV) for MoSi_2As_4 . Our detailed analysis suggests that the materials under investigation provide remarkable quantum yields, especially MoSi_2As_4 . Absence of lateral valleys, negative bright-dark splitting, and long exciton radiative lifetime give rise to high performance optoelectronic materials.

METHODS

We perform DFT calculations within the plane-wave expansion using the Quantum Espresso package⁵⁹. The gradient-corrected Perdew–Burke–Ernzerhof (PBE) functional⁶⁰ is employed together with fully relativistic norm-conserving pseudopotentials⁶¹ that account for the spin-orbit coupling. We consider as semicore states the Mo 4s and 4p orbitals, as well as the As 3d orbitals. Convergence is achieved with an 80 Ry kinetic energy cutoff and a uniform $24 \times 24 \times 1$ Monkhorst-Pack k -point mesh⁶². A 15 Å vacuum region along the c -direction, the direction perpendicular to the layer plane, is introduced to ensure decoupling of periodic replicas. The structure relaxation is assumed to have reached convergence when the maximum component of the residual ionic forces is smaller than 10^{-8} Ry/Bohr.

Building up on the obtained DFT results, we perform many-body perturbation theory calculations within the G_0W_0 approximation using the Yambo code^{63,64}. A box cutoff along the c -direction is applied to the bare Coulomb potential. The inverse dielectric matrix, $\epsilon_{\mathbf{G}\mathbf{G}'}^{-1}$, is obtained within the plasmon-pole approximation⁶⁴. We adopt the quasiparticle bandgap value at the K point as convergence parameter and fix a convergence threshold of 50 meV. Following this criterion, we employ a $36 \times 36 \times 1$ k -point mesh, 300 bands and a 10 Ry cutoff for the \mathbf{G} vectors in $\epsilon_{\mathbf{G}\mathbf{G}'}^{-1}$ and 240 bands for the computation of the correlation self-energy. In order to speed up the convergence with respect to empty states we adopted the technique described in Ref. ⁶⁵ as implemented in the Yambo code⁶⁴.

The quasiparticle band structures are then used to build and solve the Bethe–Salpeter equation on a $36 \times 36 \times 1$ k -point mesh, including eight valence and ten conduction bands in the excitonic Hamiltonian (compare the Supplementary Information).

DATA AVAILABILITY

The data supporting the findings of this study are available within the article.

CODE AVAILABILITY

No custom code is used.

Received: 29 April 2022; Accepted: 14 October 2022;

Published online: 07 November 2022

REFERENCES

- Novoselov, K. S. et al. Two-dimensional atomic crystals. *Proc. Natl Acad. Sci. USA* **102**, 10451–10453 (2005).
- Geim, A. K. & Grigorieva, I. V. Van der Waals heterostructures. *Nature* **499**, 419–425 (2013).
- Bhimanapati, G. R. et al. Recent advances in two-dimensional materials beyond graphene. *ACS Nano* **9**, 11509–11539 (2015).
- Tan, T., Jiang, X., Wang, C., Yao, B. & Zhang, H. 2d material optoelectronics for information functional device applications: status and challenges. *Adv. Sci.* **7**, 2000058 (2020).
- Kang, S. et al. 2d semiconducting materials for electronic and optoelectronic applications: potential and challenge. *2D Mater.* **7**, 022003 (2020).
- Bernardi, M., Ataca, C., Palummo, M. & Grossman, J. Electronic properties of two-dimensional layered materials. *Nanophotonics* **6**, 479–493 (2016).
- Zheng, X. & Zhang, X. Excitons in two-dimensional materials. In Thirumalai, J. & Pokutnyi, S. I. (eds.) *Advances in Condensed-Matter and Materials Physics*, chap. 2 (IntechOpen, Rijeka, 2020).
- Rasmussen, F. A. & Thygesen, K. S. Computational 2d materials database: Electronic structure of transition-metal dichalcogenides and oxides. *J. Phys. Chem. C* **119**, 13169–13183 (2015).
- Manzeli, S., Ovchinnikov, D., Pasquier, D., Yazyev, O. V. & Kis, A. 2d transition metal dichalcogenides. *Nat. Rev. Mater.* **2**, 17033 (2017).
- Nassiri Nazif, K. et al. High-specific-power flexible transition metal dichalcogenide solar cells. *Nat. Commun.* **12**, 7034 (2021).
- Bastanero, L., Cicero, G., Palummo, M. & Re Fiorentin, M. Boosted solar light absorbance in $\text{PdS}_2/\text{PtS}_2$ vertical heterostructures for ultrathin photovoltaic devices. *ACS Appl. Mater. Interfaces* **13**, 43615–43621 (2021).
- Zha, J. et al. Infrared photodetectors based on 2d materials and nanophotonics. *Adv. Funct. Mater.* **32**, 2111970 (2022).
- Taffelli, A., Diré, S., Quaranta, A. & Pancheri, L. MoS_2 based photodetectors: a review. *Sensors* **21**, 2758 (2021).
- Wang, C., Yang, F. & Gao, Y. The highly-efficient light-emitting diodes based on transition metal dichalcogenides: from architecture to performance. *Nanoscale Adv.* **2**, 4323–4340 (2020).
- Mueller, T. & Malic, E. Exciton physics and device application of two-dimensional transition metal dichalcogenide semiconductors. *npj 2D Mater. Appl.* **2**, 29 (2018).
- Robert, C. et al. Measurement of the spin-forbidden dark excitons in MoS_2 and MoSe_2 monolayers. *Nat. Commun.* **11**, 4037 (2020).
- Malic, E. et al. Dark excitons in transition metal dichalcogenides. *Phys. Rev. Mater.* **2**, 014002 (2018).
- Hong, Y.-L. et al. Chemical vapor deposition of layered two-dimensional MoSi_2N_4 materials. *Science* **369**, 670–674 (2020).
- Jian, C.-C., Ma, X., Zhang, J. & Yong, X. Strained MoSi_2N_4 monolayers with excellent solar energy absorption and carrier transport properties. *J. Phys. Chem. C* **125**, 15185–15193 (2021).
- Abdelati, M. A., Maarouf, A. A. & Fadlallah, M. M. Substitutional transition metal doping in MoSi_2N_4 monolayer: structural, electronic and magnetic properties. *Phys. Chem. Chem. Phys.* **24**, 3035–3042 (2022).
- Wang, L. et al. Intercalated architecture of MA_2Z_4 family layered van der Waals materials with emerging topological, magnetic and superconducting properties. *Nat. Commun.* **12**, 2361 (2021).
- Li, S. et al. Valley-dependent properties of monolayer MoSi_2N_4 , WSi_2N_4 , and MoSi_2As_4 . *Phys. Rev. B* **102**, 235435 (2020).
- Yao, H. et al. Novel two-dimensional layered MoSi_2Z_4 ($Z = \text{P}, \text{As}$): New promising optoelectronic materials. *Nanomaterials* **11**, 559 (2021).
- Yang, C., Song, Z., Sun, X. & Lu, J. Valley pseudospin in monolayer MoSi_2N_4 and MoSi_2As_4 . *Phys. Rev. B* **103**, 035308 (2021).
- Mortazavi, B. et al. Exceptional piezoelectricity, high thermal conductivity and stiffness and promising photocatalysis in two-dimensional MoSi_2N_4 family confirmed by first-principles. *Nano Energy* **82**, 105716 (2021).
- Nguyen, C., Hoang, N. V., Phuc, H. V., Sin, A. Y. & Nguyen, C. V. Two-dimensional boron phosphide/ MoGe_2N_4 van der Waals heterostructure: A promising tunable optoelectronic material. *J. Phys. Chem. Lett.* **12**, 5076–5084 (2021).
- Ai, H. et al. Theoretical evidence of the spin-valley coupling and valley polarization in two-dimensional MoSi_2X_4 ($X = \text{N}, \text{P}$, and As). *Phys. Chem. Chem. Phys.* **23**, 3144–3151 (2021).
- Lien, D.-H. et al. Electrical suppression of all nonradiative recombination pathways in monolayer semiconductors. *Science* **364**, 468–471 (2019).
- Kim, H., Uddin, S. Z., Higashitarumizu, N., Rabani, E. & Javey, A. Inhibited non-radiative decay at all exciton densities in monolayer semiconductors. *Science* **373**, 448–452 (2021).
- Bernardi, M., Palummo, M. & Grossman, J. C. Extraordinary sunlight absorption and one nanometer thick photovoltaics using two-dimensional monolayer materials. *Nano Lett.* **13**, 3664–3670 (2013).
- Qiu, D. Y., da Jornada, F. H. & Louie, S. G. Optical spectrum of MoS_2 : Many-body effects and diversity of exciton states. *Phys. Rev. Lett.* **111**, 216805 (2013).
- Marsili, M., Molina-Sánchez, A., Palummo, M., Sangalli, D. & Marini, A. Spinorial formulation of the GW-BSE equations and spin properties of excitons in two-dimensional transition metal dichalcogenides. *Phys. Rev. B* **103**, 155152 (2021).
- Cho, Y. & Berkelbach, T. C. Environmentally sensitive theory of electronic and optical transitions in atomically thin semiconductors. *Phys. Rev. B* **97**, 041409 (2018).
- Trolle, M. L., Pedersen, T. G. & Vénier, V. Model dielectric function for 2d semiconductors including substrate screening. *Sci. Rep.* **7**, 39844 (2017).
- Molina-Sánchez, A., Palummo, M., Marini, A. & Wirtz, L. Temperature-dependent excitonic effects in the optical properties of single-layer MoS_2 . *Phys. Rev. B* **93**, 155435 (2016).

36. Carvalho, A., Ribeiro, R. M. & Castro Neto, A. H. Band nesting and the optical response of two-dimensional semiconducting transition metal dichalcogenides. *Phys. Rev. B* **88**, 115205 (2013).
37. Kozawa, D. et al. Photocarrier relaxation pathway in two-dimensional semiconducting transition metal dichalcogenides. *Nat. Commun.* **5**, 4543 (2014).
38. Echeverry, J. P., Urbaszek, B., Amand, T., Marie, X. & Gerber, I. C. Splitting between bright and dark excitons in transition metal dichalcogenide monolayers. *Phys. Rev. B* **93**, 121107 (2016).
39. Wang, G. et al. In-plane propagation of light in transition metal dichalcogenide monolayers: optical selection rules. *Phys. Rev. Lett.* **119**, 047401 (2017).
40. Molina-Sánchez, A., Sangalli, D., Hummer, K., Marini, A. & Wirtz, L. Effect of spin-orbit interaction on the optical spectra of single-layer, double-layer, and bulk MoS₂. *Phys. Rev. B* **88**, 045412 (2013).
41. Molas, M. R. et al. Brightening of dark excitons in monolayers of semiconducting transition metal dichalcogenides. *2D Mater.* **4**, 021003 (2017).
42. Lu, Z. et al. Magnetic field mixing and splitting of bright and dark excitons in monolayer MoSe₂. *2D Mater.* **7**, 015017 (2019).
43. Palummo, M., Bernardi, M. & Grossman, J. C. Exciton radiative lifetimes in two-dimensional transition metal dichalcogenides. *Nano Lett.* **15**, 2794–2800 (2015).
44. Chen, H.-Y., Palummo, M., Sangalli, D. & Bernardi, M. Theory and ab initio computation of the anisotropic light emission in monolayer transition metal dichalcogenides. *Nano Lett.* **18**, 3839–3843 (2018).
45. Chen, H.-Y., Jhalani, V. A., Palummo, M. & Bernardi, M. Ab initio calculations of exciton radiative lifetimes in bulk crystals, nanostructures, and molecules. *Phys. Rev. B* **100**, 075135 (2019).
46. Robert, C. et al. Exciton radiative lifetime in transition metal dichalcogenide monolayers. *Phys. Rev. B* **93**, 205423 (2016).
47. Tongay, S. et al. Defects activated photoluminescence in two-dimensional semiconductors: interplay between bound, charged and free excitons. *Sci. Rep.* **3**, 2657 (2013).
48. Linhart, L. et al. Localized intervalley defect excitons as single-photon emitters in WSe₂. *Phys. Rev. Lett.* **123**, 146401 (2019).
49. Kim, J. et al. Observation of ultralong valley lifetime in WSe₂/MoS₂ heterostructures. *Sci. Adv.* **3**, e1700518 (2017).
50. Jauregui, L. A. et al. Electrical control of interlayer exciton dynamics in atomically thin heterostructures. *Science* **366**, 870–875 (2019).
51. Unuchek, D. et al. Room-temperature electrical control of exciton flux in a van der Waals heterostructure. *Nature* **560**, 340–344 (2018).
52. Zhang, C., Wang, H., Chan, W., Manolatos, C. & Rana, F. Absorption of light by excitons and trions in monolayers of metal dichalcogenide MoS₂: Experiments and theory. *Phys. Rev. B* **89**, 205436 (2014).
53. Berkelbach, T. C., Hybertsen, M. S. & Reichman, D. R. Theory of neutral and charged excitons in monolayer transition metal dichalcogenides. *Phys. Rev. B* **88**, 045318 (2013).
54. Dong, S. et al. Direct measurement of key exciton properties: Energy, dynamics, and spatial distribution of the wave function. *Nat. Sci.* **1**, e10010 (2021).
55. Mouri, S. et al. Nonlinear photoluminescence in atomically thin layered WSe₂ arising from diffusion-assisted exciton-exciton annihilation. *Phys. Rev. B* **90**, 155449 (2014).
56. Hoshi, Y. et al. Suppression of exciton-exciton annihilation in tungsten disulfide monolayers encapsulated by hexagonal boron nitrides. *Phys. Rev. B* **95**, 241403 (2017).
57. Erkensten, D., Brem, S. & Malic, E. Exciton-exciton interaction in transition metal dichalcogenide monolayers and van der Waals heterostructures. *Phys. Rev. B* **103**, 045426 (2021).
58. Lee, Y. et al. Boosting quantum yields in two-dimensional semiconductors via proximal metal plates. *Nat. Commun.* **12**, 7095 (2021).
59. Giannozzi, P. et al. QUANTUM ESPRESSO: a modular and open-source software project for quantum simulations of materials. *J. Phys.: Condens. Matter* **21**, 395502 (2009).
60. Perdew, J. P., Burke, K. & Wang, Y. Generalized gradient approximation for the exchange-correlation hole of a many-electron system. *Phys. Rev. B* **54**, 16533–16539 (1996).
61. van Setten, M. J. et al. The pseudodojo: training and grading a 85 element optimized norm-conserving pseudopotential table. *Comput. Phys. Commun.* **226**, 39–54 (2018).
62. Monkhorst, H. J. & Pack, J. D. Special points for Brillouin-zone integrations. *Phys. Rev. B* **13**, 5188–5192 (1976).
63. Marini, A., Hogan, C., Grüning, M. & Varsano, D. Yambo: an ab initio tool for excited state calculations. *Comput. Phys. Commun.* **180**, 1392–1403 (2009).
64. Sangalli, D. et al. Many-body perturbation theory calculations using the Yambo code. *J. Phys.: Condens. Matter* **31**, 325902 (2019).
65. Bruneval, F. & Gonze, X. Accurate GW self-energies in a plane-wave basis using only a few empty states: towards large systems. *Phys. Rev. B* **78**, 085125 (2008).

ACKNOWLEDGEMENTS

M.S. and U.S. acknowledge the King Abdullah University of Science and Technology (KAUST) for funding the research reported in this publication. M.S. thanks Dr. Huabing Shu and Dr. Zhiyong Zhu for helpful discussions. M.R.F. and M.P. acknowledge CINECA for high-performance computing resources under the Iskra-B initiative. M.P. acknowledges funding from Tor Vergata University through the TESLA project and INFN through the TIME2QUEST project.

AUTHOR CONTRIBUTIONS

M.S. executed the calculations under the guidance of M.P. M.R.F. and M.S. drafted the manuscript and prepared the figures. All authors contributed to the evaluation of the results and contributed to the final version of the manuscript.

COMPETING INTERESTS

The authors declare no competing interests.

ADDITIONAL INFORMATION

Supplementary information The online version contains supplementary material available at <https://doi.org/10.1038/s41699-022-00355-z>.

Correspondence and requests for materials should be addressed to Udo Schwingenschlögl or Maurizia Palummo.

Reprints and permission information is available at <http://www.nature.com/reprints>

Publisher's note Springer Nature remains neutral with regard to jurisdictional claims in published maps and institutional affiliations.



Open Access This article is licensed under a Creative Commons Attribution 4.0 International License, which permits use, sharing, adaptation, distribution and reproduction in any medium or format, as long as you give appropriate credit to the original author(s) and the source, provide a link to the Creative Commons license, and indicate if changes were made. The images or other third party material in this article are included in the article's Creative Commons license, unless indicated otherwise in a credit line to the material. If material is not included in the article's Creative Commons license and your intended use is not permitted by statutory regulation or exceeds the permitted use, you will need to obtain permission directly from the copyright holder. To view a copy of this license, visit <http://creativecommons.org/licenses/by/4.0/>.

© The Author(s) 2022